Design, Control and Evaluation of the Electro-Hydrostatic Actuator, PREHydrA, for Gait Restoration Exoskeleton Technology

Kyrian Staman, Allan J. Veale, and Herman van der Kooij

***Abstract*—A preliminary design for the PREHydrA (passive return, electro-hydrostatic actuator) concept; a high force density, remote actuator, is tested to requirements for wearable robotics technology intended for gait restoration; one of the most demanding tasks for wearable robotics. While the concept offers good wearability properties, it has never been used in wearable robotics for full support. This work shows that the combination of electro-hydrostatic actuators with a return force and series elastic element offers a good alternative to other actuation types. Custom and small commercial components are used in a design for the knee joint. An experimental setup with a pendulum representing a swinging lower leg was used to show force and angle tracking performance. The results of a maximum zero force (−400–1100 N actuator force range) tracking mean absolute error of 61 N (6.79 Nm joint torque error) at 5.5 Hz excitation and a full swing (70°) within 0.35 s (0.8 m/s actuator velocity), match or exceed current state of the art exoskeleton actuation and control and show that the PREHydrA concept is very well suited for application in exoskeleton technology, especially when the cylinder design is optimized.**

***Index Terms*—Actuation, force control, motion control, electro-hydraulics.**

I. Introduction

MANY lower limb, wearable exoskeletons for gait restoration exist, both commercially and for research: [1], [2], [3], [4], [5], [6], [7]. But they are far from restoring the full function of human legs. This challenge is due to the difficulty of control (human interaction, intention detection and balance), but also hardware needs improvement, as concluded by [8]. The need for lightweight but stiff structures, the comfortable application of high forces to a human body, devices needing to be unobtrusive and transportable and the required robustness for daily use by untrained users, all add considerable design challenges. In short; making wearable devices that can take over human functions is difficult.

Manuscript received July 13, 2020; revised October 7, 2020 and November 17, 2020; accepted November 21, 2020. Date of publication December 30, 2020; date of current version February 22, 2021. This article was recommended for publication by Associate Editor J. Patton and Editor P. Dario upon evaluation of the reviewers' comments. This work was supported by the Netherlands Organization for Scientific Research (NWO), under Project 14429. *(Corresponding author: Kyrian Staman.)*

The authors are with the Department of Biomechanical Engineering, University of Twente, 7522 NB Enschede, The Netherlands (e-mail: k.staman@utwente.nl; a.j.veale@utwente.nl; h.vanderkooij@utwente.nl).

Digital Object Identifier 10.1109/TMRB.2020.3048224

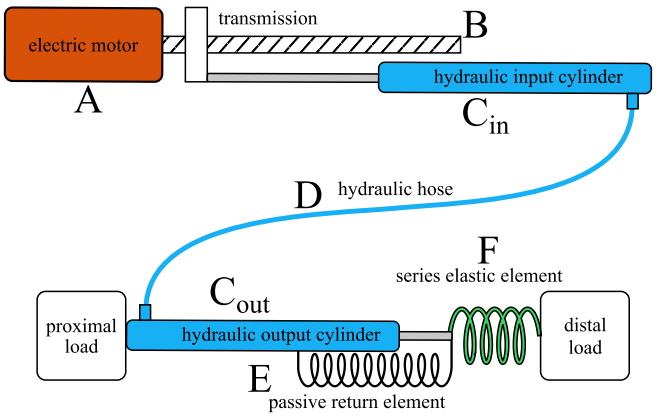

Fig. 1. Schematic of the PREHydrA concept, with electric motor (A), linear transmission (B), and input cylinder (C_{in}). The flexible hydraulic transmission (D), output cylinder (C_{out}), passive return element (E), and series elastic element (F) are placed between a proximal and distal body segment spanning a joint.

An important aspect is the actuators that deliver controlled power to the device, generating forces and motions to perform tasks. Actuators are usually the largest source of mass in a device and thus can limit the wearability considerably.

In previous work we [9] presented the PREHydrA (passive return, electro-hydrostatic actuator) shown in Figure 1 as an actuator concept for wearable robotics as an improvement over electromechanical, Bowden cable and conventional (valved) hydraulic actuators. With the relocation of the motor and transmission to the wearer's back, the mass distribution improves over linear and rotary electromechanical actuators, a practice that is also observed in systems using Bowden cable transmissions. These systems, however, suffer from low force efficiencies and difficulty of control due to heavy, nonlinear, configuration-dependent friction [10], [11]. This can be circumvented by using a fluid transmission, but conventional fluid power systems suffer from serious inefficiency, due to valves throttling the flow [12], hence the choice for a hydrostatic actuator. The goal was to develop a high force density actuator, using remote actuation to relocate mass to favorable locations to improve the wearable aspect.

Others [13] have tried to use small scale hydraulics as well, but mostly with low forces, low velocities and low pressures (often using pneumatic components). The downside is that this results in systems with a low force density only able to deliver partial support. The exoskeleton actuation systems that

This work is licensed under a Creative Commons Attribution 4.0 License. For more information, see https://creativecommons.org/licenses/by/4.0/

can deliver high forces and thus full support ([1], [14], [15]), mostly use conventional hydraulic solutions (pressure reservoir and valves) which quickly become heavy due to the many components and inefficient due to the throttling of pressure. The PREHydrA concept was shown to produce high output forces over a range of frequencies relevant to wearable robotics, but the question remains if it can meet the dynamic requirements of lower limb exoskeletons. The design hypothesis is that adding control, designed for a linearized system, and design of return and series elastic elements, will result in an actuator that meets the requirements of gait. To this end two common control approaches in wearable robotics are applied and the performance evaluated.

This article evaluates the ability of the PREHydrA concept to be controlled to produce the full forces and velocities required for level ground gait restoration, with experimental validation in a proof of concept test setup for knee joint requirements, specifically. It's main contribution, although just a step in the process of developing small-scale hydrostatic actuation systems for wearable robotics, is accurate, full joint torque (as opposed to partial support) and motion control on hardware with a novel return force element.

Requirements for the actuator will be derived in the next section. The detailed design of passive return and series elastic elements is presented in the section Actuator Design, control design in the section Control and results obtained from an experimental setup in the Experimental Results section. This article presents a discussion of the obtained results at the end and ends with a conclusion.

II. Requirements

The most common task of lower limb exoskeletons is straight, level ground walking (chosen here at 1 m/s, which is slow for the average human, but fast for current state of the art exoskeletons). Indicative average joint torques and angles were experimentally determined by [16] for the sagittal plane. Analysis showed that the highest range of motion is found in the knee joint (about 65°) as well as the highest velocity and acceleration. The torque profile of the knee (for an 80 kg subject) is similar to the hip, where the ankle joint has a three times higher torque during stance. The torque profile for the ankle is mostly unidirectional, while the knee and hip joints require both positive and negative torques. The frequency content of gait motions and torques is up to about 4 Hz and is directly proportional to the walking speed.

Placement of the actuators was symmetric with respect to the joint and as shown in Figure 2. The actuator locations were chosen such that pushing actuator forces (actuator in compression) deliver the maximum joint torques to make use of the high forces hydraulics can deliver. Note that actuator elongation corresponds to a negative joint angle, so positive actuator motion and force corresponds to extension of the hip and knee joint and plantar flexion for the ankle. The configuration parameters (h and d) were estimated based on the size of small commercially available cylinders (see Experimental Setup section).

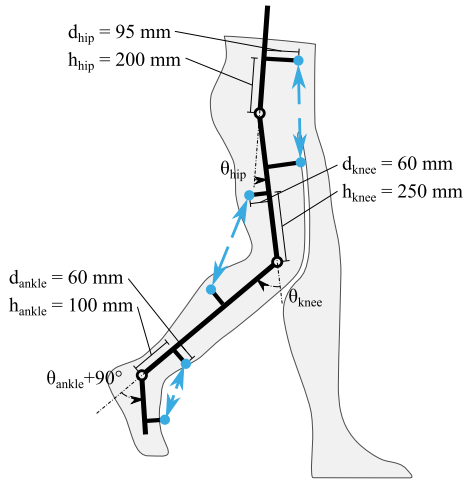

Fig. 2. Symmetric linear actuator configuration in the sagittal plane on the right leg. Actuator forces acting on the exoskeleton structure in blue.

TABLE I
Actuator Requirements for Presented Configuration

	stroke (m)			velocity (m/s)	force (N)
hip	0.060	stance	max	0.175	380
			min	−0.253	−425
		swing	max	0.084	189
			min	−0.314	−196
knee	0.142	stance	max	0.135	465
			min	−0.889	−300
		swing	max	0.892	40
			min	−0.807	−337
ankle	0.029	stance	max	0.234	1780
			min	−0.104	−90
		swing	max	0.035	14
			min	−0.135	−63

Translating the joint requirements to the actuators resulted in similar observations as done by analysis of gait data. The large range of motion of the knee joint now resulted in a significantly higher actuator velocity for the chosen configuration. The actuator requirements for the three joints for the given configuration are shown in Table I, split in swing and stance gait phases.

The average moment arms (over a gait cycle, using the configuration shown in Figure 2) were 107 (75 to 130), 110 (60 to 185) and 61 (35 to 74) mm for the hip, knee and ankle joint actuators, respectively. Placing the actuator closer to the joint reduced the required velocity and would be more favorable for hydraulic cylinders. In this work, the size of the commercial cylinders prevented a more favorable configuration.

From these requirements the large stroke of the knee actuator demands high dynamic performance, especially during swing, which complicated the design. The high force of the ankle is less of a challenge, since hydraulic actuators are well suited to deliver high forces in less dynamic conditions (during stance). Furthermore, the direction of this force (pushing off, or actuator extension) causes it to have little influence on the return element. Therefore, in this work, the application of the actuator to the knee joint was investigated, the first part of which was to design the passive return element for the required force.

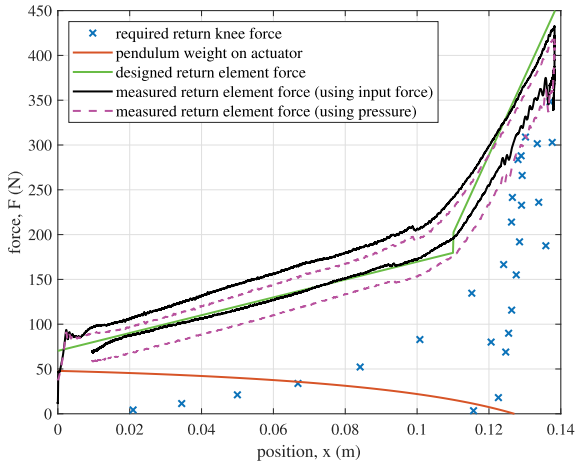

Fig. 3. Return force with Amatec T32890 (modified) and Amatec E1000-115-2750M springs in series, plotted with knee actuator force requirement.

III. Actuator Design

In previous work the actuator was designed and tested in a test setup with a spring load [9]. There the proximal and distal load (see Figure 1) were the fixed world and there was no distinction between series elastic element and passive return element. The setup presented in this work uses the same components, but now the distal load is dynamic (a swinging leg/pendulum). Other than that, the passive return element and the series elastic element were designed specifically for the derived requirements for the knee joint.

A. Passive Return Element

As shown in Figure 1, the hydrostatic transmission is unidirectional (single-acting) and requires a passive return element to generate motion and force in the opposite direction (actuator retraction). This removes the need for an additional fluid line and the friction, sealing, mass, volume, deaeration and difficult filling that come with it, but there are two main limitations. First, the maximum return force that can be produced depends on actuator displacement and second, the force requirements for the electric motor are increased, because elastic energy needs to be stored for when return force is delivered. The former can be compensated by pretensioning the elastic element, but this increases the latter limitation. So, the return element should be carefully designed for a given application.

From the gait data of [16] and the actuator configuration for the knee, the return force (actuator force generating a knee flexion torque) required over the range of motion of the actuator was calculated. This return force is shown in Figure 3; it is made positive for clarity. Note that only a high return force is required when the actuator is almost fully extended. This corresponds to flexing the knee at the onset of the swing phase during gait.

Note also that the knee swing actuator force requirement of 337 N (without the minus sign) is directly shown in the figure. It is clear that if the return element can exert this force, the requirement is met.

A two spring design was used for the return element as shown in Figure 4. Two springs generate the return force

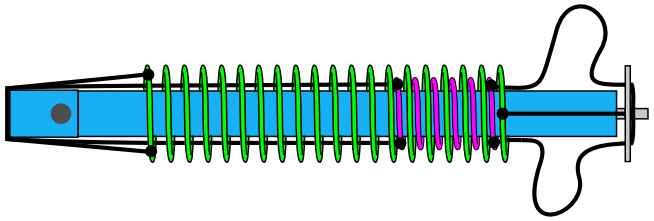

Fig. 4. Return element implementation. The full stroke spring (green) and end of stroke spring (purple) are mounted using cords (black) around the cylinder (blue). Cords where knotted (black dots) to a small metal helical ring inserted into the first coil of the springs (not shown for clarity).

(indicated by the green line in Figure 3) over the entire range of motion; a low stiffness spring over the entire range of motion and a stiffer spring engaged only when the actuator extended beyond 110 mm using a simple Dyneema cord. The low stiffness spring was a modified commercially available spring (see Table II), cut in half to provide about twice the stiffness (1 kN/m) with sufficient stroke remaining. The stiffness of the end of stroke spring was significantly higher with 7.76 kN/m. The pretension of the full stroke spring allows the actuator to fully retract against the friction of the cylinders and any static loading (such as the pendulum described in the Experimental Setup section). This is seen in the force offset at $x = 0$.

An experiment was carried out to verify the stiffness characteristic of the return element. The system was extended with a low constant velocity (15 mm/s), kept at maximum position for 2 seconds and retracted with the same velocity. The input force (between transmission and hydraulic input cylinder, see Figure 1) and pressure halfway the hydraulic hose were measured. During the experiment the spring force is equal to the friction of both cylinders minus the measured input force. The friction was experimentally characterized by [9]. The measured pressure was assumed to be equal in the output cylinder and thus the spring force is equal to the friction of the output cylinder minus the force generated by the pressure. The black and magenta lines in Figure 3 show the experimentally identified return element force using the input force and pressure, respectively.

Figure 3 shows that the identified stiffness of the full stroke spring corresponded well with the model, the end of stroke spring was slightly more compliant, but still provided sufficient force over its range of motion. The observed hysteresis was a combined effect of cord dissipation, fluid effects (like friction and deaeration) and mechanical backlash, but was not investigated, since the return element's performance was sufficient.

B. Series Elastic Element

Series elastic actuators can benefit from improved force control bandwidth and fidelity and lower high frequency impedance (see [17]); all properties that are beneficial to human wearable robotics. There are many examples of series elastic actuation being used in exoskeleton technology, prostheses and rehabilitation devices, but the stiffness varies strongly, because different devices were designed for

different tasks and loads. But even for devices designed for the same task, there is no clear cut answer as to how stiff it should be. For example, the iT-Knee [18] has a stiffness of 1000 Nm/rad, while a device with a similar use case, the Assist-On Knee [19], only has a stiffness of 26 Nm/rad. Other examples are the KIT-EXO [20] (between 600 and 696 Nm/rad), the AwAS [21], which can render a stiffness between 30–1300 Nm/rad, and the AwAS-II [22] with even more uncertainty (anything between 0 and rigid), the LOPES gait trainer [23] (155 Nm/rad increased to 388 Nm/rad during experiments), dos Santos' device [24] (105 Nm/rad), and Stuhlenmiller's [25] knee actuator (296 Nm/rad). Finally, the Mindwalker exoskeleton [26] documents a spring stiffness of 800 Nm/rad and the Symbitron exoskeleton actuators have a spring stiffness of 1534 Nm/rad [27].

In this work, a linear spring stiffness of 58 kN/m was used to obtain an average rotational stiffness (with the average moment arm of 110 mm) of about 700 Nm/rad. As no exoskeleton was proposed in this work, the series elastic element was integrated in the actuator.

The design of the series elastic element incorporated two compression springs for forward and backward motion. The output cylinder piston connected to the input shaft of the series elastic element, which was guided by a support housing that housed the springs. The stroke of the springs was 8 mm in both directions, resulting in a maximum force of 464 N which was sufficient for the actuator force requirement of 337 N. A load cell was mounted after the series elastic element.

IV. Control

For actuators used in wearable robotic systems it is useful to be able to control the interaction force between actuator and wearer [28]. The main performance metric of the presented actuator concept was the accuracy of tracked representative forces in the presence of friction and unmodeled (or inaccurately modeled) system characteristics. As shown in Figure 5, this was the output force, F_{out}. To compensate for cylinder friction, the electric motor plus ball screw (M) used an internal feedback controller to control the velocity of the motor and input cylinder piston, v_{in}, (rigidly attached to the ball screw). The force feedback controller, C_F, supplies the desired velocity control signal, u_v.

Besides force control, many exoskeleton applications prescribe the motion of the user as summarized by [28]. Therefore, a (pendulum) motion controller was also tested, as shown in Figure 6, consisting of a pendulum angle (θ_p) feedback (PD) controller, C_θ, and a feedforward component, FF, which was a force compensating the weight of the pendulum. The feedback controller was cascaded around the force control loop.

A. Model Linearization

In order to better understand the system and apply linear control theory the different nonlinearities are analyzed and linearized for the purpose of deriving linear control plant transfer functions.

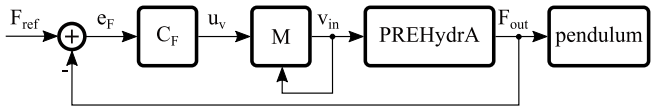

Fig. 5. Block diagram of the output force control strategy, based on a reference force, F_{ref} and force error, e_F. M denotes the motor drive controllers and hardware, connected to the PREHydrA and pendulum.

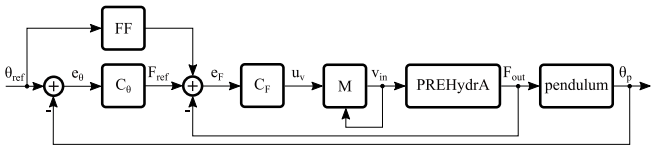

Fig. 6. Block diagram of the pendulum motion control strategy, based on a reference angle, θ_{ref} and angle error, e_θ. M denotes the motor drive controllers and hardware, connected to the PREHydrA and pendulum.

In Figures 5 and 6 two critical signals are omitted (for clarity) that introduce some complexity into the systems. First, from the PREHydrA subsystem (which contains the hydraulics' friction, inertia and unidirectionality), there is an interaction force between the input cylinder piston and the ball screw (contained in M). This is the force that the load (pendulum) generates on the fluid (in the PREHydrA block) and is transmitted to the electric motor, M, across the ball screw. This force, since the fluid column transmits it, is unidirectional; a fluid column can only be in compression. A large enough negative input piston velocity (the motor pulls quickly and with high force on the input piston) would create a vacuum between input piston and fluid and subsequently cause deaeration of the hydraulic fluid. Something that is highly undesirable for system performance and is difficult to model correctly.

This nonlinear behavior can be neglected entirely if the return element is sufficiently strong (delivers enough compression force) such that the fluid is never uncompressed. This was verified in simulation and no significant difference in force tracking performance is observed between a bidirectional acting system with the return element dimensioned as described before and a system where a simple unidirectionality is added (forcing the fluid interaction force to be positive).

Furthermore, modeling of the nonlinear behavior of the return element itself does not significantly influence the derived plant transfer functions. The effect of a changing stiffness is completely compensated by closing the velocity feedback loop.

Second, the pendulum angular motion causes the housing of the series elastic element to move. In other words; the series elastic spring compression (and thus output force F_{out}) is caused on one hand by the output cylinder motion (contained in the PREHydrA block) and on the other hand by the pendulum motion. Calculating the spring deflection on the pendulum side is a nonlinear function of the pendulum angle, since it is the anti-derivative of the moment arm. A trigonometric function gives the moment arm:

$$r(\theta_p) = \sqrt{h_{knee}^2 + d_{knee}^2}\,\sin\left(\tan^{-1}\left(\frac{d_{knee}}{h_{knee}}\right) + \frac{20\pi/180 - \theta_p}{2}\right)$$

In which the moment arm is calculated from the configuration parameters, h_{knee} and d_{knee} (as shown in Figure 2) in m

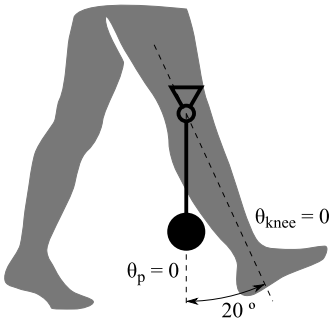

Fig. 7. Schematic representation of the pendulum with respect to the knee joint.

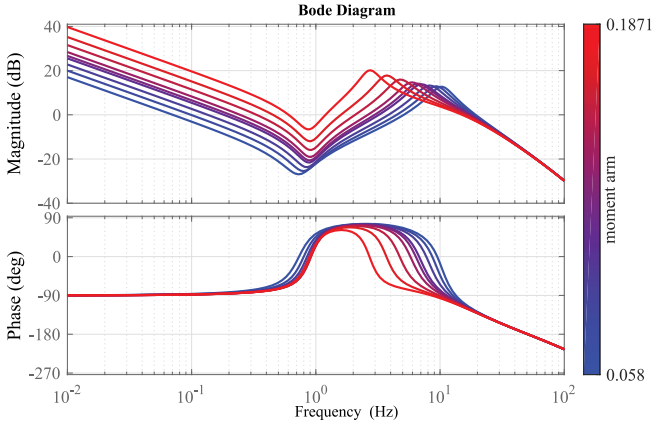

Fig. 8. Bode diagram of the force plant transfer function, u_v to F_{out}, for different moment arms.

and the pendulum angle θ_p in rad. This is derived from a straightforward trigonometric analysis of the knee joint. Note the 20° offset between pendulum angle, θ_p, and knee angle ($\theta_{knee} = 20 - \theta_p$), that matches the pendulum orientation with that of a leg in swing. This is shown in Figure 7.

The moment arm is also multiplied by the output force to find the torque acting on the pendulum, so this geometric nonlinearity is introduced twice in the system; from PREHydrA to pendulum block and back. Let's assume a constant moment arm. Figures 8 and 9 show the transfer functions of the control plants for the output force and pendulum angle controlled systems respectively, calculated for different values across the entire range of possible moment arms.

Figure 8 shows that the changing moment arm does not influence the location of the anti-resonance at 0.8 Hz much, which is caused by the pendulum eigenfrequency. The eigenfrequency caused by pendulum inertia and series elastic spring, between 3 and 10 Hz changes significantly. The force controller to be designed must maintain robust stability and performance for this plant.

Closing the force control loop with the controller, as presented in a later section, and deriving the angle plant shows less influence of a changing moment arm. Closing the feedback loop compensates the low frequency gain shift.

Neglecting the effect of pendulum motion on the series elastic spring and assuming a fixed load system (like others have done; see for example [29]) when controlling the output force, is in this case not a valid assumption. As shown in Figure 10, removing the pendulum dynamics from the plant

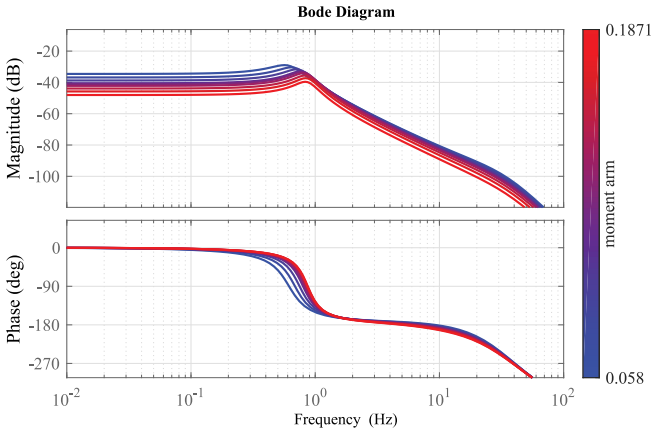

Fig. 9. Bode diagram of the motion plant transfer function, $F_{ref} + FF$ to θ_p, for different moment arms.

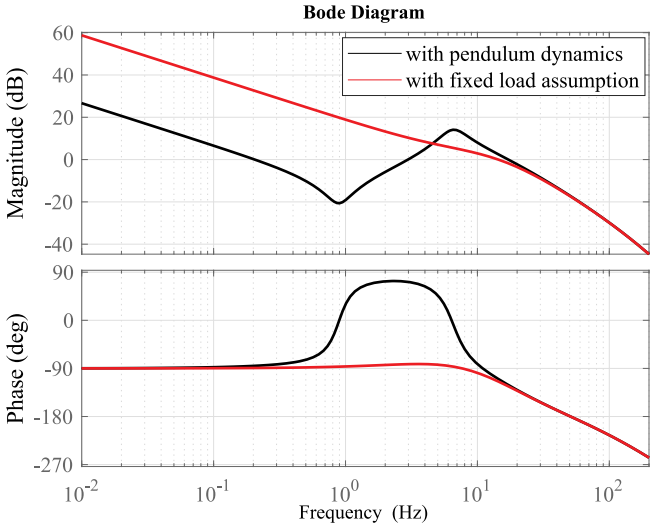

Fig. 10. Bode diagram of the force plant transfer functions, u_v to F_{out}, for the moment arm at −16°, for a system with a dynamic load (pendulum) and a fixed load.

transfer function of the force controlled system results in a significant change in the low frequency behavior up to about 10 Hz. Assuming a fixed pendulum does not make sense for the motion controlled system.

Lastly, gravity is neglected from the pendulum model in the derivation of transfer functions.

B. Inner Loop Force Controller

Loop shaping techniques were used to obtain a bandwidth of 30 Hz with 50° phase margin, based on the linearized control plant with a constant moment arm at a pendulum angle at −16° (the average angle during swing). This bandwidth should be significantly higher than the outer loop (a generally used rule of thumb is three to four times higher) to prevent interference between the loops. The high inner loop bandwidth will also reduce the impedance of the system. The resulting controller was a proportional integral derivative (PID) controller with leaky integrator and finite derivative of the

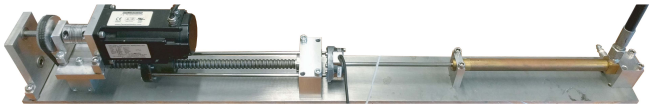

Fig. 11. Photograph of the test setup input stage, components 2–15 from Table II.

Fig. 12. Photograph of the test setup output stage, components 15–21 from Table II.

form:

$$C_F = k_F \frac{s + z_{i,F}}{s + p_{i,F}} \frac{s + z_{d,F}}{s + p_{d,F}}$$

where k_F is the proportional gain of 1.77×10^{-2} m/Ns, $p_{i,F}$ the integrator pole at 1.89 rad/s (0.3 Hz) to prevent saturation and $z_{i,F}$ a zero at 100.5 rad/s (16 Hz). The derivative zero, $z_{d,F}$, is also located at 100.5 rad/s and its pole, $p_{d,F}$, caps the derivative action at 1005 rad/s (160 Hz).

With the force controller and the linearized plant, the output impedance transfer function, defined here as the transfer from pendulum angle, θ_p, to output force, F_{out}, can be modeled, as shown in the Results section, Figure 15.

C. Outer Loop Motion Controller

A low-pass filter was added to the motion controller to reduce the effects of angular encoder noise and quantization. The bandwidth was set at only 5 Hz, which is sufficient for gait motion of the knee, with a phase margin of 30°.

$$C_\theta = k_\theta \frac{s + z_{d,\theta}}{s + p_{d,\theta}} \frac{p_f}{s + p_f}$$

where k_θ is the proportional gain of 1.35×10^4 N/rad. The derivative zero, $z_{d,\theta}$ and the pole, $p_{d,\theta}$ are at 10 and 100.5 rad/s (1.6 and 16 Hz) respectively. The filter pole, p_f, is set at 63 rad/s (10 Hz).

The gravitational torque of the pendulum is relatively easy to compensate using a feedforward strategy. Translating this torque to actuator space (a translational force) is done by calculating and dividing by the actuator moment arm as shown in the equation:

$$FF = \frac{mgl \sin(\theta_{ref})}{r(\theta_{ref})}$$

where the numerator is the gravitational torque, defined by the pendulum mass, $m = 4$ kg, times the gravitational acceleration, $g = 9.81$ m/s^2, times the effective pendulum length, $l = 0.4$ m, times the sine of the pendulum angle; in this case the reference angle, θ_{ref} in rad. The denominator is the moment arm, as estimated from the reference angle.

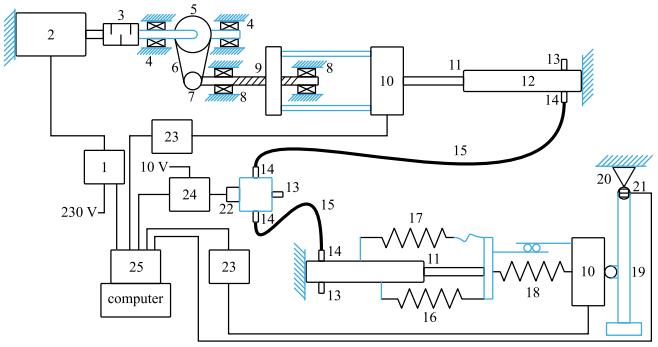

Fig. 13. Schematic representation of test setup components; commercial components are numbered and listed in Table II, components in blue are custom parts.

TABLE II
EXPERIMENTAL SETUP COMMERCIAL COMPONENTS

#	*Component*
1	Kollmorgen S20260-VTS, 240 V AC, brushless servo drive
2	Kollmorgen AKM22C-BCNC-00, 0.84 Nm, 290 W servomotor
3	Ruland PCMR25-8-8-A aluminium flexible coupling
4	SKF W628/8 R-2Z flanged deep groove ball bearing
5	RS Pro MXL025 80 teeth timing pulley
6	RS Pro MXL 115 teeth timing belt
7	RS Pro MXL025 40 teeth timing pulley
8	SKF 7200 BEP angular contact ball bearing
9	Misumi BSSR1405-325-RLC, 5 mm lead, rolled ball screw
10	ATI mini45-E six-axis force/torque transducer
11	Clippard H9C-6D brass cylinders (modified)
12	Eurol Coolant XL -36, 50% ethane-1,2-diol coolant
13	generic M6 threaded car brake bleed screw
14	Parker GE08LR1/8EDOMD, male stud connector
15	Parker 550H, 0.5 m thermoplastic hydraulic hose
16	Amatec T32890, 0.5 kN/m extension spring (modified)
17	Amatec E1000-115-2750M, 7.76 kN/m extension spring
18	Amatec D12940, 58.35 kN/m compression spring
19	THN MB 010.010 DU cylindrical plain bearing
20	2 SKF SYWR 30 YTHR Y-bearing plummer block units
21	RLS RMB28V10BS10 angular magnetic encoder module
22	Measurement Specialties EPX-N02-150B-Z2 pressure sensor
23	ATI 9105-IFPS-1 DAQ interface power supply
24	ICP DAS SG-3016 conditioning module
25	National Instruments 6225 M-series DAQ PCI card

V. EXPERIMENTAL SETUP

An experimental setup was developed using a pendulum with inertia (0.48 kgm^2) about the rotation axis equivalent to a human lower leg, a mass of 4 kg and a length of 0.4 m. Photographs of the input stage and output on the pendulum are shown in Figures 11 and 12. A schematic representation of the setup is shown in Figure 13, with the components listed in Table II.

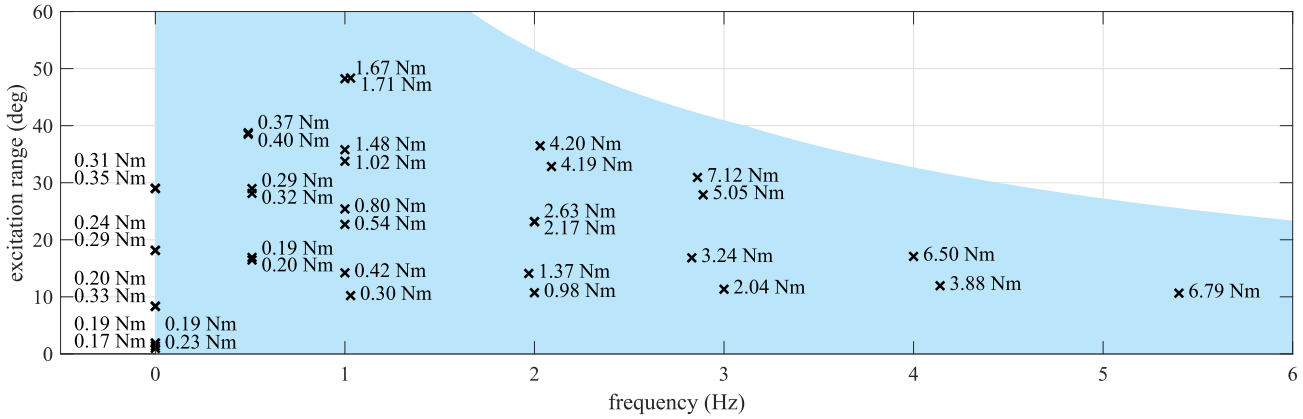

Fig. 14. Mean absolute torque tracking errors estimated from force and angle measurements. Note that reference signals at 0 Hz are constant force tracking experiments of −50, −40, −25 and 0 N from top to bottom.

Careful filling and air bleeding of the system was important to ensure the incompressibility of the PREHydrA's fluid column. The setup's design facilitated this process. The highest point in the setup was the connector block (where the pressure sensor is located, see Figure 13, component 22) located halfway along the fluid hose. A bleed screw was integrated in this connector block to allow for air bleeding both during and after filling. Two identical bleed screws were integrated into the commercial cylinders and were used as filling points. Filling the system from the cylinder chambers up into the hose and out of the top bleed screw ensured that a minimal amount of air was trapped in the system. After initial filling, the setup was moved back and forth to allow any remaining air to make its way up to the bleed screw; the air was bled from the system and a small amount of hydraulic fluid was inserted by syringe to fully fill the system. This second procedure was repeated as maintenance at the start of a set of experiments. The data acquisition computer shown in Figure 13 was a dedicated Simulink Real-Time target computer which executed the control models generated from Simulink.

VI. Experimental Results

The first experiment was actuator force tracking, using the force control strategy shown in Figure 5. This actuator force was equal to the force in the series elastic element and was directly measured by the output cylinder load cell (component 10 in Figure 13). The force tracking error was then compared to a model of the output impedance. Second, motion control experiments, using the motion controller as shown in Figure 6, were performed to investigate the velocity requirement of 0.892 m/s. This maximum velocity occurs during the swing phase, when the lower leg swings through the entire range of motion of the knee.

A. Force Tracking

The first 10 experiments consisted of constant force tracking of −50, −40, −25 and 0 N output forces. The pendulum's initial position is at the minimum angle of −0.7565 rad (−43.8°), due to the return element being designed to retract the pendulum against gravity (see Actuator Design section). A slow ramp reference starts off from the initial measured force of −57.2 N (the weight of the pendulum on the actuator) to the desired constant value over 3 seconds. The resultant equilibrium angle is shown as the pendulum "excitation range" in Figure 14 and, since the experiments end in equilibrium, they are shown at an excitation frequency of 0 Hz. Some tracking error is observed due to sensor noise, stick slip behavior and spring oscillations.

A further 27 experiments were performed with a sinusoidal input motion provided to the pendulum. This was done manually on the beat of a metronome to get a constant input motion frequency and care was taken to get a constant motion amplitude.

The results for all experiments at various frequencies and amplitudes are shown in Figure 14, where the excitation range is the peak-to-peak amplitude of the provided motion. The blue area is the operational area of the actuator, limited by physical end stops of the setup and maximum motor velocity.

It can be seen that the tracking error becomes larger for increasing range of motion and frequency. Because the amplitude of the excitation was kept as close to the pendulum zero angle (straight down) as possible, a larger range of motion means that the actuator was further extended and the return element delivered a higher return force that the actuator had to compensate. Figure 3 shows that the return force was about 180–350 N. As expected, the tracking performance decreases for higher frequencies.

Comparing the same 27 experimental data sets to the modeled impedance (see Figure 15) shows a slightly higher measured impedance than the model predicted. The modeled impedance transfer function assumed a constant moment arm between actuator and pendulum and was calculated for the minimum and maximum moment arms (lower bound corresponds to minimal moment arm), resulting in the area shown in Figure 15 in which the output impedance was expected to fall. The almost factor 2 deviation between model and experiments could have been caused by sensor noise and quantization, which was not taken into account in the model and degraded control performance. Physical factors like friction, play and model parameter deviations also caused an underestimate from the model, but it was still useful to predict the system's behavior.

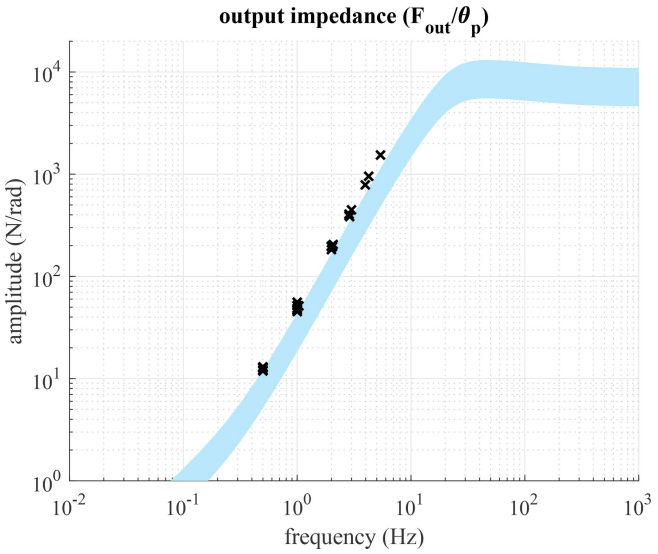

Fig. 15. Calculated impedance from force tracking experiments, compared to modeled impedance transfer range for varying moment arm (blue area).

In terms of joint impedance (torque tracking error in Nm), the conversion from actuator force was done by estimating the torque (real-time) from the measured force and calculating a moment arm from the measured pendulum angle. Although the multiplication of both noisy signals is inaccurate, the mean absolute torque tracking errors indicated good performance, as shown in Figure 14. By comparison, [27] showed estimated output impedances between 10–15 Nm (between 0.1 and 8 Hz) with state of the art force control for full support lower-limb exoskeleton (electromechanical) actuators. Compared to Bowden cable actuators, [30] reports a mean absolute tracking error of about 0.34 Nm for 0.125 Hz, 60° motion in a tethered knee exoskeleton (a device with similar maximum force capabilities). Extrapolating from experiments shown in Figure 14 at 0.5 Hz shows similar performance.

B. Motion Tracking

Five experiments were performed on the pendulum setup with a "skewed" sine reference motion of various step times, t_{step}, of 3, 2, 1, 0.5 and 0.35 s:

$$\theta_r(t) = \theta_0 + \frac{\theta_f - \theta_0}{t_{step}} t - \frac{\theta_f - \theta_0}{2\pi} \sin\left(\frac{2\pi}{t_{step}} t\right)$$

where θ_r is the angle reference in radians as a function of time, t, in s. The angles θ_0 and θ_f are the initial and final angles, of -0.765 rad ($-43.8°$) and 0.175 rad (10°) respectively. In the top graph of Figure 16, the reference motion profiles are shown with the closed loop tracking data, using the control strategy shown in Figure 6. A comparison was made with model simulations, taking into account the nonlinear effects of the system. This showed a slight underestimation in the overshoot at the highest velocities.

For the various step times, the maximum velocities were calculated from the angular reference signal to be 0.63, 0.94, 1.88, 3.75, and 5.36 rad/s. With the moment arm as a function of angle the actuator velocities become 0.087, 0.13, 0.26, 0.52,

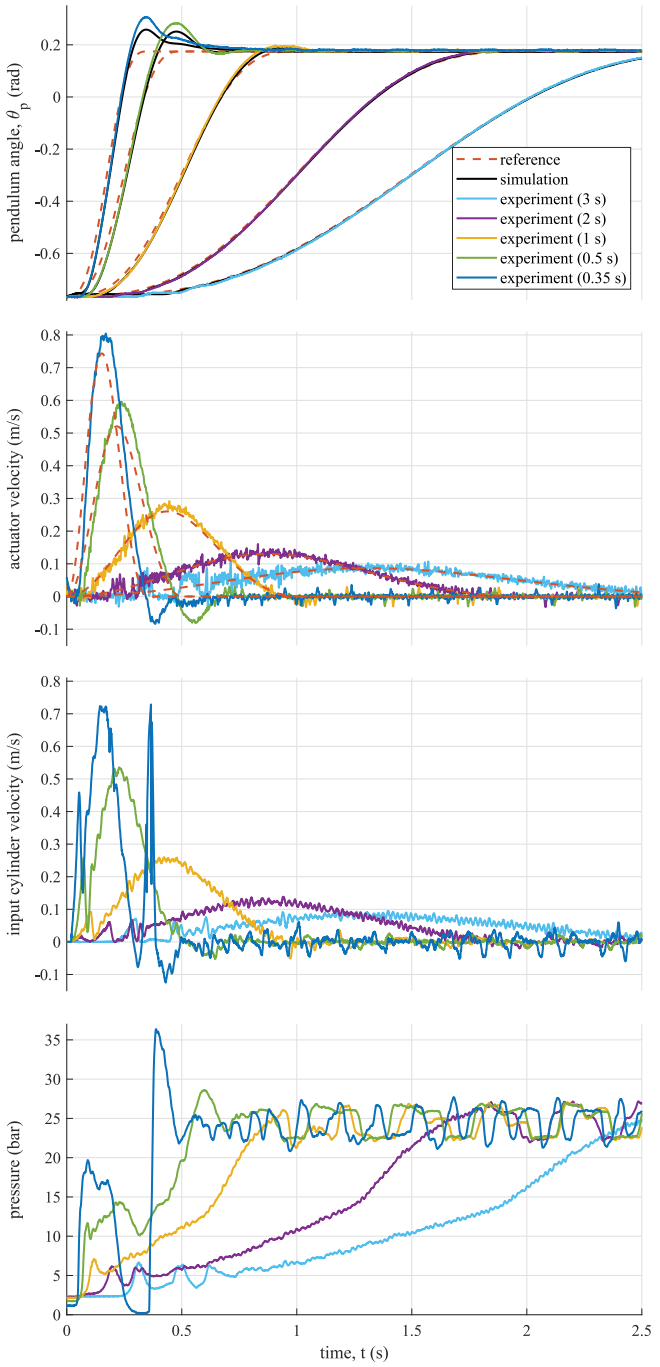

Fig. 16. Motion tracking experiments for various step references. Top: measured pendulum angle compared to simulation. Second: velocity of actuator output cylinder, calculated from pendulum motion. Third: velocity of actuator input cylinder, calculated from motor encoder. Bottom: absolute pressure measurement.

and 0.74 m/s, respectively, falling just short of the required 0.892 m/s (see Table I), which would be obtained with a step time of 0.29 s. Taking the filtered (forward and reverse pass through a first order, 50 Hz low pass filter to compensate phase lag) measured angle and its numerical derivative also allowed computation of the actuator velocity, which is shown in the second graph of Figure 16, where the actual (measured) velocity was slightly higher (maximum 0.8 m/s) due to the overshoot of the setup.

The overshoot limited further reduction of the step time, and thus increase in velocity, because the pendulum began to hit its mechanical end stop, despite implementation of software end stops. This effect was already seen for the 0.35 s step time when the input cylinder velocity is calculated from the electric motor encoder as shown in the third graph of Figure 16. The sharp velocity peak, although it did not deteriorate motion tracking performance, is undesirable and was assumed to be caused by some performance limit or interaction between the series elastic spring, the return element and the software end stop. Just before this velocity peak, the bottom graph of Figure 16 shows a pressure drop to almost below 0 bar, which would mean pulling on the fluid column and consequently deaeration. The 0.35 second experiment is the limit of performance of the setup and can only be improved by a stronger return force element or specific solutions to deal with the rapid deceleration of the pendulum at the end of its swing.

VII. Discussion

The goal of this work was to test the proposed actuator concept for application in wearable robotics. Both the implementation of hardware and the performance of force and position control. And although the results show the validity of the PREHydrA concept, there are a few points to be discussed.

First, it should be noted that the [16] data set, although it gives a reasonable estimate of velocities and torques in human gait, is not more than that; a rough estimate. With only 19 data points describing the average swing torques and joint angles of 19 human subjects, it lacks temporal resolution, making derivatives inaccurate, and in averaging the joint angles no variance can be determined for the joint velocities. Other data sets, like [31], might be better suited to derive more accurate specifications, but that was not the intent of this work. The actuator requirements therefore serve more as an estimate than strict requirements.

Second, the actuator requirements are heavily dependent on the configuration of the actuators and since no device is proposed, the configuration is a rough estimation. For the knee, the mentioned commercial cylinder can be used, but its length makes it highly unsuited for hip and knee actuation. Requirements for those joints were estimated by assuming custom cylinders can be manufactured and mounted close to the leg.

It should also be noted that smaller cylinders, mounted closer to the joint will not only improve the wearable aspect of the actuators (lower mass, higher force density, smaller envelope), but also reduce the velocity and increase force requirement. This requires a less dynamic actuator, which favors a hydraulic option. The minimum orifice size that the hydraulic fluid needs to pass through limits scaling, so velocity reduction is beneficial here as well. Smaller hoses and couplings mean less mass and volume. Ideal design of the cylinders should prevent leakage while still minimizing friction losses. Higher leakage will result in a system that needs to compensate for lost fluid or needs to be easily filled or serviced by the user. More friction losses will result in a poorer energy efficiency, requiring a stronger motor and more stored electrical energy. Commercial cylinders usually favor friction over leakage, but for custom designs this analysis should be performed.

Since this actuation concept involves the miniaturization of existing technologies, the cost of implementation with not differ significantly from other types of actuators. Its complexity and amount of components is similar to any other unidirectional actuator and does not require the valves and other pressure regulating components of conventional hydraulics, reducing its cost relative to that.

The design of the dual spring return element is as effective as it is simple. Selecting springs that can be nested (full stroke spring around end of stroke spring around cylinder) made for a compact design and attachment through cords allowed for easy adjustment of the pretension and engagement distance of the end of stroke spring. Performance during experiments was constant and robust after initial assembly.

The series elastic element design performed sufficiently well, but ideally should not introduce any "dead" length in the actuator. Using a single spring in both compression and extension could reduce its length of about 60 mm, but a better recommendation is to integrate the series elastic element into the joint of a device that is to be actuated. Especially if a constant rotational series stiffness is desired. Since the moment arm of the actuator changes with joint angle, the joint stiffness also changes. The smaller the joint angle (knee stretched), the lower the stiffness. This is undesired for the knee joint during gait, since during the stance phase a higher stiffness is probably necessary.

Although the system contained a few sources of nonlinear behavior (unidirectionality, the return element, a configuration-dependent moment arm, and pendulum gravitational torque), analysis and simulation showed good performance and robustness with a linear control design approach. If performance needs to be improved, it might be necessary to look into gain scheduling, feedback linearization or other methods of compensating nonlinear behavior, especially for the output force controlled system, which suffers the most from the nonlinearity of the changing moment arm.

Experimental results show that the proposed force control strategy works well for compensation of (primarily) cylinder friction, in combination with a series elastic element, for a unidirectional actuator and in a geometrically nonlinear configuration. Furthermore, a model that assumes a constant moment arm predicts the system's behavior well enough for mechanical and control design. Finally, the accuracy with which an interaction force between wearable device and human needs to be controlled in order to "feel good" is heavily dependent on many device and application specific factors as shown by [8], but the obtained results presented are expected to be a good basis.

The control of the pendulum motion shows good performance for lower velocities, but the two fastest experiments show a few degrees overshoot which limited performance on the current setup and preventing it from reaching the required velocity. This requires careful analysis of the requirements on actuators for human gait, because if humans

end the swing phase by swinging the lower leg into physiological "end stops" of the knee joint, then the force requirements derived from gait data sets are insufficient for preventing devices to hit mechanical end stops. The cascaded motion control strategy, although it can be straightforwardly added to the force control strategy, might not be the best performing. The force control loop limits the achievable bandwidth and with it the possibility of higher gain feedback, which would reduce the observed overshoot.

Future work will focus on the design of small scale components (primarily cylinders) to find an optimum balance between force and velocity requirements and improve the wearability of the system. Miniaturization and integration of the electric motor-transmission-input cylinder system has already started, with a first prototype mass below 1.6 kg for the high force requirement of the ankle.

VIII. Conclusion

Here, the PREHydrA concept is tested to demonstrate the dynamic force and position control performance for requirements derived from restoration of gait; a key contribution in its realization as an actuation system for wearable robotics. Its components were implemented, modeled and evaluated in a test setup for a single task; a human knee joint during the swing phase of gait. This task was selected for its high requirement on dynamic performance. Experimental results show good performance, with a maximum zero force tracking mean absolute error of 61 N (6.79 Nm) at 5.5 Hz excitation. The velocity requirement was not completely fulfilled, reaching a maximum velocity of 0.8 m/s of the required 0.89 m/s. This was due to limitations of the pendulum and not the actuator. According to the estimated requirements the PREHydrA is also likely suited for actuation of the hip and ankle joints and possibly for upper limb wearable robotics. This makes the PREHydrA a remote actuator suited to produce the high forces required for full support wearable robotics.

References

[1] A. B. Zoss, H. Kazerooni, and A. Chu, "Biomechanical design of the Berkeley lower extremity exoskeleton (BLEEX)," *IEEE/ASME Trans. Mechatronics*, vol. 11, no. 2, pp. 128–138, Apr. 2006.

[2] R. Griffin *et al.*, "Stepping forward with exoskeletons: Team IHMC's design and approach in the 2016 Cybathlon," *IEEE Robot. Autom. Mag.*, vol. 24, no. 4, pp. 66–74, Dec. 2017.

[3] J. Choi, B. Na, P.-G. Jung, D.-W. Rha, and K. Kong, "WalkON suit: A medalist in the powered exoskeleton race of Cybathlon 2016," *IEEE Robot. Autom. Mag.*, vol. 24, no. 4, pp. 75–86, Dec. 2017.

[4] T. Gurriet *et al.*, "Towards restoring locomotion for paraplegics: Realizing dynamically stable walking on exoskeletons," in *Proc. IEEE Int. Conf. Robot. Autom.*, May 2018, pp. 2804–2811.

[5] T. Vouga, R. Baud, J. Fasola, M. Bouri, and H. Bleuler, "TWIICE—A lightweight lower-limb exoskeleton for complete paraplegics," in *Proc. Int. Conf. Rehabil. Robot.*, 2017, pp. 1639–1645.

[6] C. Meijneke, S. Wang, V. Sluiter, and H. van der Kooij, "Introducing a modular, personalized exoskeleton for ankle and knee support of individuals with a spinal cord injury," in *Wearable Robotics: Challenges and Trends*. Cham, Switzerland: Springer, 2017, pp. 169–173.

[7] A. Esquenazi, M. Talaty, A. Packel, and M. Saulino, "The ReWalk powered exoskeleton to restore ambulatory function to individuals with thoracic-level motor-complete spinal cord injury," *Amer. J. Phys. Med. Rehabil.*, vol. 91, no. 11, pp. 911–921, 2012.

[8] M. del Carmen Sanchez-Villamañan, J. Gonzalez-Vargas, D. Torricelli, J. C. Moreno, and J. L. Pons, "Compliant lower limb exoskeletons: A comprehensive review on mechanical design principles," *J. Neuroeng. Rehabil.*, vol. 16, no. 1, p. 55, 2019.

[9] K. Staman, A. J. Veale, and H. van der Kooij, "The PREHydrA: A passive return, high force density, electro-hydrostatic actuator concept for wearable robotics," *IEEE Robot. Autom. Lett.*, vol. 3, no. 4, pp. 3569–3574, Oct. 2018.

[10] D. Chen, Y. Yun, and A. D. Deshpande, "Experimental characterization of Bowden cable friction," in *Proc. IEEE Int. Conf. Robot. Autom.*, May 2014, pp. 5927–5933.

[11] Y. Lee *et al.*, "Biomechanical design of a novel flexible exoskeleton for lower extremities," *IEEE/ASME Trans. Mechatronics*, vol. 22, no. 5, pp. 2058–2069, Oct. 2017.

[12] A. Zoss and H. Kazerooni, "Architecture and hydraulics of a lower extremity exoskeleton," in *Proc. ASME Int. Mech. Eng. Congr. Expo.*, Nov. 2005, pp. 1447–1455.

[13] R. A. Bos, K. Nizamis, D. H. Plettenburg, and J. L. Herder, "Design of an electrohydraulic hand orthosis for people with Duchenne muscular dystrophy using commercially available components," in *Proc. 7th IEEE Int. Conf. Biomed. Robot. Biomechatronics*, 2018, pp. 305–311.

[14] K.-T. Park and H. M. Kim, "Wearable robotic system using hydraulic actuator," in *Proc. 11th Int. Conf. Control Autom. Syst.*, 2011, pp. 1697–1701.

[15] H. Kim, C. Seo, Y. J. Shin, J. Kim, and Y. S. Kang, "Locomotion control strategy of hydraulic lower extremity exoskeleton robot," in *Proc. IEEE Int. Conf. Adv. Intell. Mechatronics*, 2015, pp. 577–582.

[16] D. A. Winter, *Biomechanics and Motor Control of Human Movement*. Hoboken, NJ, USA: Wiley, 2009.

[17] J. Pratt, B. Krupp, and C. Morse, "Series elastic actuators for high fidelity force control," *Ind. Robot Int. J.*, vol. 29, no. 3, pp. 234–241, 2002.

[18] L. Saccares, I. Sarakoglou, and N. G. Tsagarakis, "iT-Knee: An exoskeleton with ideal torque transmission interface for ergonomic power augmentation," in *Proc. IEEE/RSJ Int. Conf. Intell. Robots Syst. (IROS)*, 2016, pp. 780–786.

[19] B. Celebi, M. Yalcin, and V. Patoglu, "AssistOn-Knee: A self-aligning knee exoskeleton," in *Proc. IEEE/RSJ Int. Conf. Intell. Robots Syst.*, 2013, pp. 996–1002.

[20] J. Beil, G. Perner, and T. Asfour, "Design and control of the lower limb exoskeleton KIT-EXO-1," in *Proc. IEEE Int. Conf. Rehabil. Robot. (ICORR)*, 2015, pp. 119–124.

[21] A. Jafari, N. G. Tsagarakis, B. Vanderborght, and D. G. Caldwell, "A novel actuator with adjustable stiffness (AwAS)," in *Proc. IEEE/RSJ Int. Conf. Intell. Robots Syst.*, 2010, pp. 4201–4206.

[22] A. Jafari, N. G. Tsagarakis, I. Sardellitti, and D. G. Caldwell, "A new actuator with adjustable stiffness based on a variable ratio lever mechanism," *IEEE/ASME Trans. Mechatronics*, vol. 19, no. 1, pp. 55–63, Feb. 2014.

[23] H. Vallery, J. Veneman, E. van Asseldonk, R. Ekkelenkamp, M. Buss, and H. van der Kooij, "Compliant actuation of rehabilitation robots," *IEEE Robot. Autom. Mag.*, vol. 15, no. 3, pp. 60–69, Sep. 2008.

[24] W. M. dos Santos, G. A. P. Caurin, and A. A. G. Siqueira, "Design and control of an active knee orthosis driven by a rotary series elastic actuator," *Control Eng. Pract.*, vol. 58, pp. 307–318, Jan. 2017.

[25] F. Stuhlenmiller, "Design of an elastic actuation system for a gait-assistive active orthosis for incomplete spinal cord injured subjects," M.S. thesis, Biomed. Eng. Res. Centre, Universitat Politècnica de Catalunya, Barcelona, Spain, 2016.

[26] S. Wang, C. Meijneke, and H. van der Kooij, "Modeling, design, and optimization of Mindwalker series elastic joint," in *Proc. IEEE 13th Int. Conf. Rehabil. Robot. (ICORR)*, 2013, pp. 1–8.

[27] W. F. Rampeltshammer, A. Q. L. Keemink, and H. van der Kooij, "An improved force controller with low and passive apparent impedance for series elastic actuators," *IEEE/ASME Trans. Mechatronics*, vol. 25, no. 3, pp. 1220–1230, Jun. 2020.

[28] A. J. Young and D. P. Ferris, "State of the art and future directions for lower limb robotic exoskeletons," *IEEE Trans. Neural Syst. Rehabil. Eng.*, vol. 25, no. 2, pp. 171–182, 2016.

[29] N. Paine *et al.*, "Actuator control for the NASA-JSC Valkyrie humanoid robot: A decoupled dynamics approach for torque control of series elastic robots," *J. Field Robot.*, vol. 32, no. 3, pp. 378–396, 2015.

[30] S. Yu *et al.*, "Design and control of a high-torque and highly backdrivable hybrid soft exoskeleton for knee injury prevention during squatting," *IEEE Robot. Autom. Lett.*, vol. 4, no. 4, pp. 4579–4586, Oct. 2019.

[31] J. K. Moore, S. K. Hnat, and A. J. van den Bogert, "An elaborate data set on human gait and the effect of mechanical perturbations," *PeerJ*, vol. 3, Apr. 2015, Art. no. e918.